Geophysical Research Letters

RESEARCH LETTER
10.1029/2026GL124117

Ground-Truthed Fiber-Optic Sensing Reveals Internal Tide Bores Over Madeira's Steep Slope

Matthew H. Alford[1], Mohammad Belal[2,3], Alberto C. Naveira Garabato[4], Carl Spingys[2], Gunnar Voet[1], Oleg A. Godin[5], Ernst M. Uzhansky[5], Jennifer Ward Neale[2], Jesus Reis[6,7], and Afonso Loureiro[6,7]

[1]Scripps Institution of Oceanography, University of California San Diego, La Jolla, CA, USA, [2]National Oceanography Centre, Southampton, UK, [3]Electronics and Computer Science, University of Southampton, Southamptont, UK, [4]Ocean and Earth Science, University of Southampton, Southampton, UK, [5]Naval Postgraduate School, Monterey, CA, USA, [6]ARDITI – Agência Regional para o Desenvolvimento da Investigação Tecnologia e Inovação, Observatório Oceânico da Madeira, Funchal, Portugal, [7]Instituto Dom Luiz - Faculdade de Ciências - Universidade de Lisboa, Lisboa, Portugal

Key Points:

- We present the first near-bottom validation of DAS-inferred temperature using yoyo-CTD measurements reaching 5–10 m above the seafloor
- Regressions yield an empirical DAS temperature sensitivity of 21–37 μstrain K^{-1}, 2.5–4× greater than simple theoretical values
- The combined DAS + yoyo-CTD data reveal internal-tide bore dynamics on a steep slope, demonstrating a powerful combined approach

Supporting Information:

Supporting Information may be found in the online version of this article.

Correspondence to:

M. H. Alford,
malford@ucsd.edu

Citation:

Alford, M. H., Belal, M., Naveira Garabato, A. C., Spingys, C., Voet, G., Godin, O. A., et al. (2026). Ground-truthed fiber-optic sensing reveals internal tide bores over madeira's steep slope. *Geophysical Research Letters*, *53*, e2026GL124117. https://doi.org/10.1029/2026GL124117

Received 2 MAY 2026
Accepted 26 JUN 2026

Abstract

We demonstrate the combined utility of distributed acoustic sensing (DAS) and repeat conductivity-temperature-depth (CTD) profiling for observing internal tide dynamics over a sloping seafloor. While DAS has been widely proposed as a method to infer ocean temperature variability from seafloor cables, quantitative in situ validation has been limited. Here we present the first published detailed comparison between DAS-inferred bottom temperature fluctuations and near-bottom temperature measured from high-resolution yoyo-CTD time series reaching 5 m above the seafloor, conducted over the EllaLink/GeoLab cable on the slope of Madeira. Linear regressions yield an empirical DAS temperature sensitivity of 21–37 μstrain K^{-1}, a factor 2.5–4 greater than commonly used theoretical estimates. The calibrated DAS record reveals semidiurnal internal tide bores propagating upslope to ∼1,300 m depth, where propagation halts and transitions to a complex interference pattern. These observations highlight the potential of combining seafloor fiber sensing with targeted in situ profiling to observe near-bottom internal tide breaking processes.

Plain Language Summary

Optical fibers in seafloor telecommunication cables can be used as sensors to detect temperature and motion in the ocean. However, it has been difficult to verify what these signals mean using direct ocean measurements nearby. We compare temperature inferred from a fiber-optic seafloor cable to repeated shipboard profiles taken within meters of the seabed near the island of Madeira. The comparison allows us to estimate how strongly the DAS signal responds to temperature changes, and shows that the sensitivity differs from simple theoretical predictions. Using this calibration, the fiber reveals internal tide bores moving upslope and interacting with Madeira's steep seabed in a highly complex way. The results show that combining fiber-optic sensing with targeted shipboard profiling provides a powerful new method to observe energetic near-bottom ocean processes.

1. Introduction

Distributed optical fiber sensing (DOFS) has the potential to greatly alleviate our current vast undersampling of the ocean (Naveira Garabato, Spingys, Lucas, et al., 2025). By sending laser light down optical fibers such as those in seafloor communication cables, the light backscattered from density fluctuations in the fiber's glass can be used to infer a variety of properties—primarily temperature and strain—of the fiber and its surroundings. Since the speed of light in glass is well known, returns can be accurately associated with distance along the fiber, giving measurements as functions of time and along-cable distance. Better still, fiber strain is sensitive to acoustic pressure, enabling long arrays of hydrophone-like measurements that could in principle be used with ambient ocean sound to constrain the temperature and velocity structure of the water column above the fiber (Godin, 2006; Wu et al., 2020).

The feasibility of such prospects depends on a better characterization of the fiber's temperature and strain responses under real ocean conditions. A number of papers have presented distributed acoustic sensing (DAS) signals that appear consistent with ocean processes including mesoscale eddies (Pelaez Quiñones et al., 2023), calving glaciers (Gräff et al., 2025), internal waves (Williams et al., 2023) and turbulence (Spingys et al., 2024). While Pelaez Quiñones et al. (2023) compared low-frequency fiber-inferred temperature to a mooring 4 km away, we are not aware of any published studies prior to this one with in situ measurements close enough for detailed internal tide comparisons as presented here.

Here we address this validation gap by comparing DAS phase measurements from theGeoLab seafloor fiber near Madeira with near-bottom temperature variability measured directly using repeat yoyo-CTD profiling reaching 5–10 m above the seabed. This comparison enables an empirical estimate of the effective DAS temperature sensitivity under real seafloor installation conditions. We then use the calibrated DAS record to image the multi-scale evolution of internal tide bores propagating and reflecting over Madeira's steep slope. Together, these results demonstrate how fiber sensing and targeted in situ profiling can be combined to resolve near-bottom internal wave processes at spatiotemporal scales not achievable with conventional approaches.

2. Experiment and Methods

The Madeira Fiber Optical Groundtruthing (M-FOG) experiment seeks to deploy a variety of in situ oceanographic instruments near the GeoLab seafloor cable (Emacom/EllaLink) at Madeira in order to explore the potential and limits of distributed acoustic sensing, as well as to compute the "transfer functions" between measured optical phase and both temperature (this paper) and acoustic pressure (other papers in progress). The expected temperature sensitivity, which is reviewed in Supporting Information S1, is complicated even for an idealized, unshielded fiber, and is even more so for real seafloor armored cables (Budiansky et al., 1979; Hartog et al., 1979; Hocker, 1979; Sidenko et al., 2022; Sinnett et al., 2020).

The comparisons took place at the GeoLab dark fiber (Loureiro et al., 2025) extending ∼57 km southeastward from Funchal, Madeira (Figure 1). The narrow insular shelf and steep upper slope of Madeira allow the GeoLab cable to sample the shelf–slope–deep-ocean continuum along a single cross-slope fiber segment. We focus on four tidally resolving "yoyo" conductivity-temperature-depth (CTD) stations. Three of the stations (Table 1) were 12–13 hr (approximately one semidiurnal tidal cycle) in length and conducted during our first cruise from 26 October to 2 November, 2025, with a top-to-bottom profile performed every hour. Station 3 was reoccupied for 2.5 days (approximately 5 semidiurnal cycles) on our mooring recovery cruise in January 2026. Much better time resolution (≈7 min) was achieved by cycling only to 400 m above the seafloor. All casts on both cruises were performed to within 5–10 m of the seafloor through use of an altimeter.

Optical phase data were sampled at 500 Hz using an ASN OptoDAS interrogator installed at the Emacom Praia Formosa Cable Landing Station, in Funchal. Following standard practice, the raw phase data output by the interrogator are expressed first as "effective strain" ϵ^* following the equations in Supporting Information S1. For display in this paper, they are then converted to "fiber-inferred temperature" using a value $\partial\epsilon^*/\partial T = 32.2$ μstrain K^{-1}. This value, a central result of our paper, is determined below via linear least-squares regression against temperature directly measured from CTD station 3 (Table 1), 5–10 m above and ≈800 m to the side of the cable. As described in Supporting Information S1, this inferred sensitivity is several times larger than the nominal value expected from simple first principles considerations, highlighting the need for improved theory for real cables.

For the analyses in this paper, two 2.5-day periods were extracted by low-pass filtering the 500 Hz data with a 2-s time constant and downsampling into 2 s intervals, giving sample and Nyquist frequencies of 0.5 and 0.25 Hz, respectively. The first period was from October 29 to 1 November 2025, spanning the CTD stations and the beginning of the moored measurements, while the second one took place in 23–26 January, 2026 coinciding with the longer yoyo-CTD time series.

3. Results

3.1. Fiber Data

Fiber-inferred temperature during the October period (Figure 2, bottom) is first plotted over 6–14 km along-cable distance (600–2300 m water depth; see distance markers in Figure 1). Several features are immediately apparent. First, motions are predominantly semidiurnal, showing upslope-propagating internal tides. These signals weaken and become non-propagating inshore of 8.25 km, which we argue in the Discussion is likely due to reflection at the steep slope. Second, near the 1,600 m isobath, the cable spans two high points on the seafloor, making it much more sensitive to ocean flow. Such spanning segments have been used elsewhere to detect turbulence (Loureiro

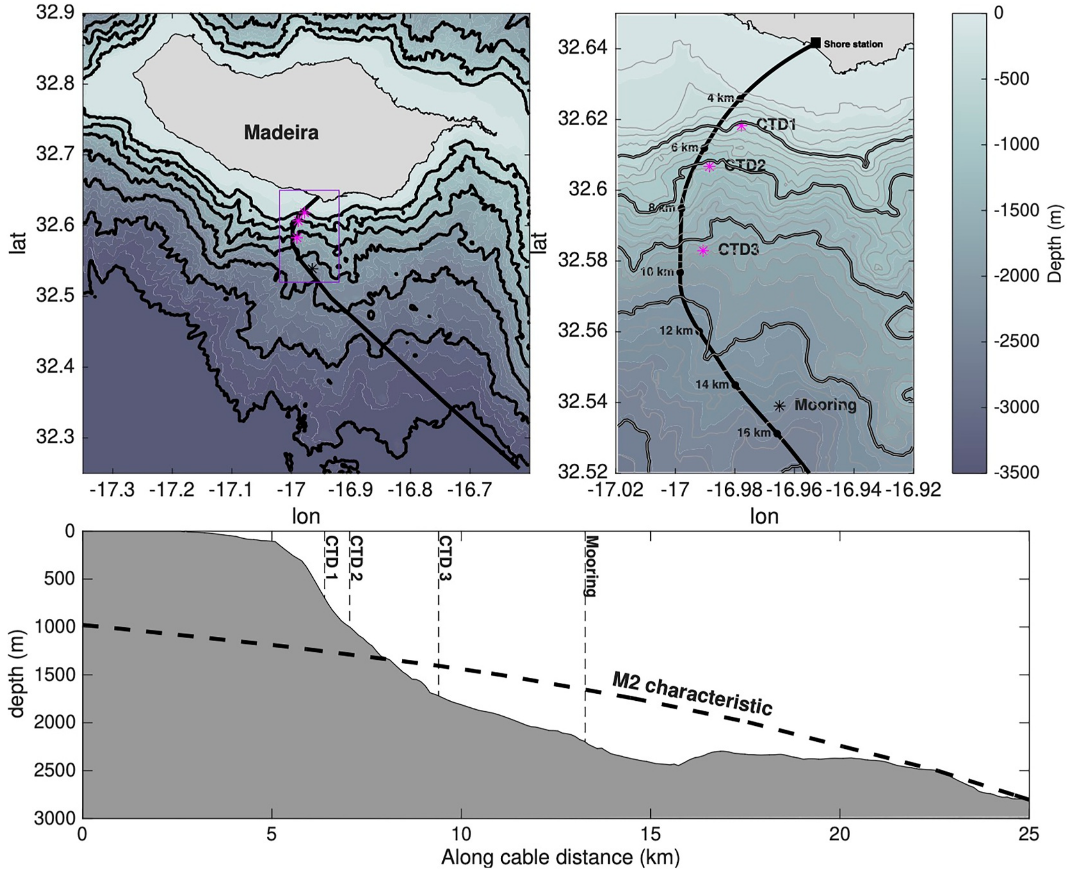

Figure 1. (Upper left) Regional map showing bathymetry near the island of Madeira, the fiber extending down the slope from Funchal and our moored and shipboard stations. Contour interval is 500 m. (Upper right) A zoom in of the boxed region at left, showing the more detailed bathymetry near the cable in the depth range of interest in this paper. Contour interval is 500 m (thick) and 100 m (thin). Note the fiber location and the CTD locations are approximate, though the relative distances in Table 1 are correct. (bottom) Bathymetric cross section along the cable and station locations. A characteristic of the M_2 internal tide is overplotted, demonstrating the supercriticality of the upper part of the slope and the expectation for strong reflection of the internal tide near the 1,300 m isobath, as observed in the fiber data.

et al., 2025; Spingys et al., 2024), but we will ignore them here. Third, a marked set of lighter-colored vertical bands is evident, which we speculatively interpret as buried and therefore less-sensitive segments of the fiber.

3.2. Fiber/in Situ Temperature Comparisons

The inferred bottom temperature from the optical fiber is compared with near-bottom temperature from three 13-hr-long in situ hydrographic time series collected on the October cruise (Table 1 and Figure 2, upper panels) and a longer station on the January cruise (Figure 3). In each panel pair in both figures, CTD temperature in the lower 400 m is shown in the upper panels, and temperature at the deepest extent of each cast is plotted below

Table 1
Station Information and Fit Coefficients

Station	Depth	$\overline{T}$(°C)	$\partial\epsilon^*/\partial T$ (μstrain K^{-1})	R^2	Dist. from cable (m)
1, 30–31 Oct, 2025	700 m	11.2	21.3 (13.6–50.2)	0.40	563
2, 29 Oct, 2025	1,000 m	9.3	37.0 (13.3–48.1)	0.12	78
3, 29–31 Oct, 2025	1,722 m	5.9	35.7 (22.5–92.3)	0.68	814
3, 24–26 Jan, 2026	1,722 m	5.86	32.2 (29.3–35.7)	0.61	814

Note. Sensitivity values in parentheses are the 95% confidence limits determined from the regression fits.

10.1029/2026GL124117

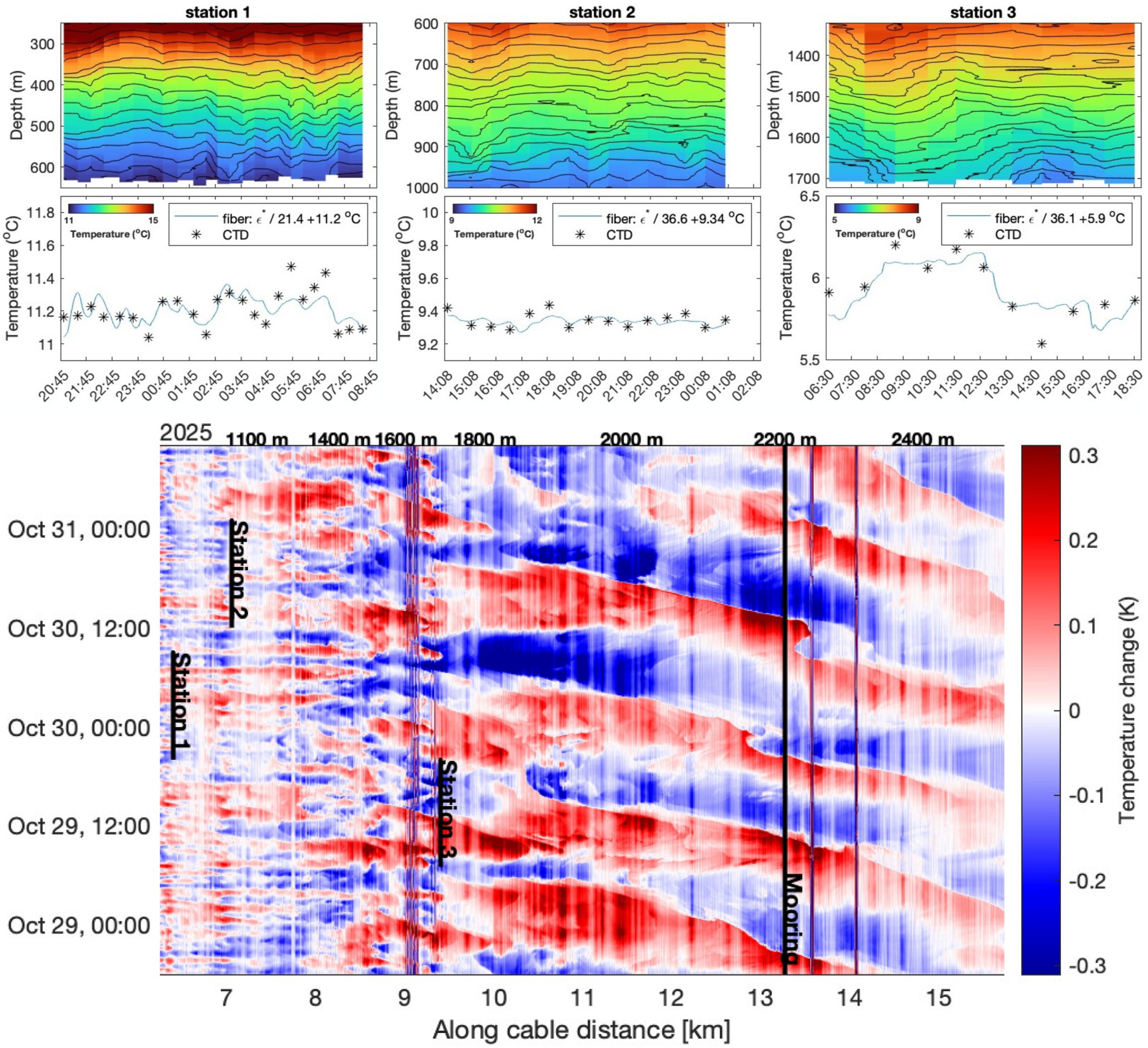

Figure 2. Fiber and CTD comparisons. (top) Time/depth series of temperature from yoyo stations conducted at locations in Figure 1. (middle) Temperature from the deepest bottom approach of the CTD (black; 5–10 m from bottom) and fiber (blue), using the fit data shown in the legend and in Table 1. (bottom) Temperature change inferred from the fiber using $\partial\epsilon^*/\partial T$ 32.2 μstrain K^{-1}. With this value, the color bar limits correspond to $\epsilon^* = \pm 10$ μstrain. The locations and times of the CTD stations plotted above are shown with vertical lines, and selected water depths of the cable are indicated at top.

(black dots). Although single CTD stations cannot detect phase propagation as can the fiber, the reduced amplitude of inshore near-bottom temperature fluctuations evident in Figure 2 is indeed replicated in the shallower two stations (stations 1–2). Fiber and CTD signals at these stations are not obviously tidal, in contrast to the deeper 1,700 m station 3 (upper right), where regular, vigorous vertical displacements of semidiurnal frequency are seen, particularly in the longer time series (Figure 3).

At each station, the mean and offset between the fiber strain data and CTD near-bottom temperature are determined by linear least-squares regression (Figure 2, middle panels). Fiber strain data ϵ^* (Supporting Information S1) are interpolated onto the time base of the approximately hourly near-bottom temperature measurements from the CTD (black dots), and the time mean $\overline{T}$, slope $(\partial\epsilon^*/\partial T)^{-1}$ and R^2 values computed. These results are summarized in Table 1. The temperature range plotted in the middle panels is the same for all stations,

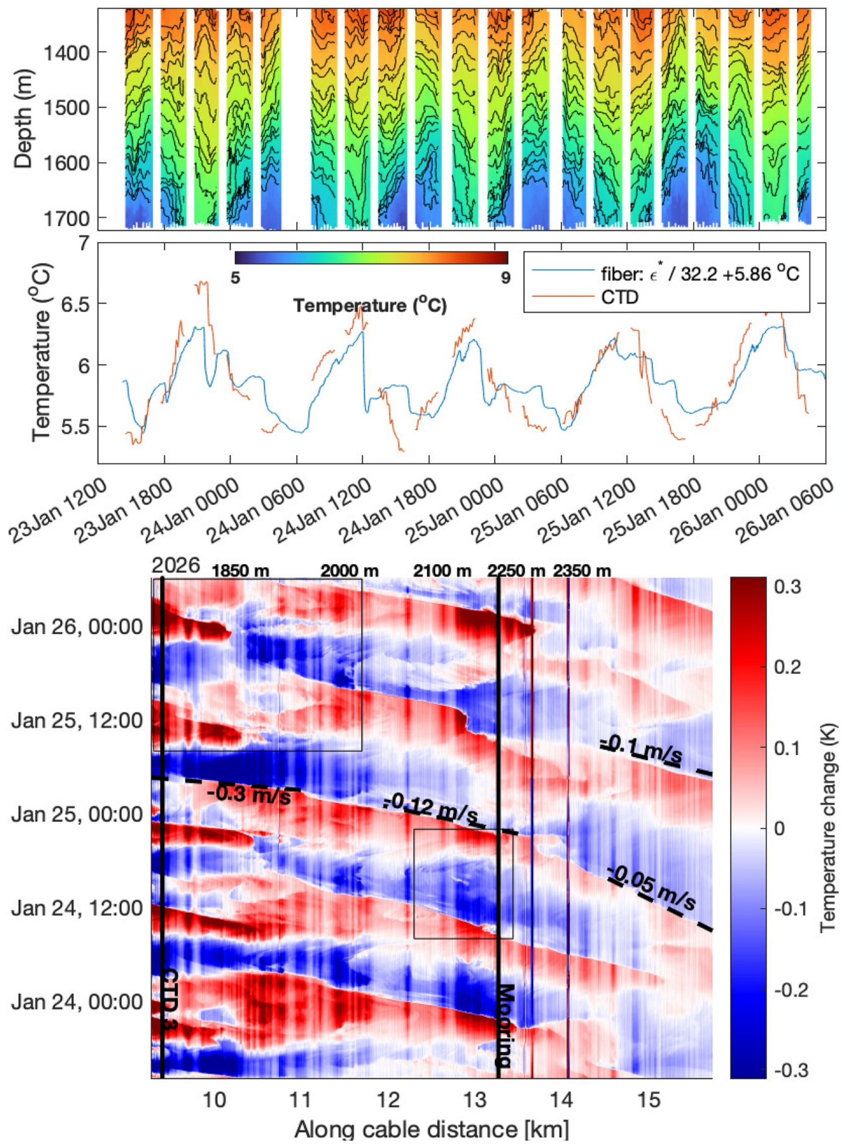

Figure 3. Fiber and CTD comparisons for the January 2026 occupation of station 3. (top) Temperature versus depth and time measured from the yoyo-CTD time series. (middle) Deepest temperature from each cast of the CTD (5–10 m above bottom; red) and inferred temperature from fiber data at that isobath using the fit data shown in the legend and in Table 1. (bottom) As in Figure 2 but for January 2026 and zoomed in for kilometers 9–16. Slanted dashed lines are representative propagation speeds.

demonstrating the greatly reduced amplitude as well as the less obvious dominance of the semidiurnal tide at the shallower two stations.

The hourly sampling and single semidiurnal tidal cycle spanned by the October stations give large error bars on the regression coefficients (Table 1), though the estimated sensitivities are still larger than the theoretical value of 9 μstrain K^{-1} (Supporting Information S1) at the 95% confidence level. A more detailed comparison with smaller error bars is possible at station 3, which was sampled for more time and more frequently in January 2026 (Figure 3). In order to focus on the portion of the slope where the internal tide is propagating upslope, fiber data in Figure 3 are only plotted for along-cable distances >9 km. The non-propagating signals and the greater amplitudes at the spanning section are similar to those in Figure 2. In January 2026, the CTD was cycled only in the lower 400 m except for an excursion to the surface each 2 hrs (Figure 3, upper panel, white gaps and middle panel, gaps in red line). Except during these periods, time between bottom approaches was about 7 min compared to 1 hr for the stations shown in Figure 2.

The $\partial\epsilon^*/\partial T$ values computed from the regressions are $\approx$32 μstrain K^{-1} for the deeper stations and $\approx$21 μstrain K^{-1} for the shallower station. These values are 2.5–4 times greater than the rough theoretical value of 9 μstrain K^{-1} (Supporting Information S1). Agreement between fiber and CTD data varies among stations, with the shallowest stations exhibiting lower explained variance (Table 1). This likely reflects a combination of (a) increased spatial decorrelation between the CTD site and the fiber segment in regions of strong along-slope variability, and (b) differences between temperature variability at the seafloor (sensed by the cable) and at 5–10 m above bottom (sampled by the CTD) in the presence of a stratified and intermittently turbulent bottom boundary layer (see Discussion). In addition, localized burial of the cable by the surrounding sediment may have reduced the effective thermal response at the shallowest station, explaining the lower sensitivity.

3.3. Internal Tide Bore Propagation From the Combined Fiber/CTD Data Set

Having computed an empirical calibration between the fiber and the CTD, we now discuss internal tide features in the combined data set. Visual agreement at the January occupation of station 3 is strong, though with some important differences that are discussed below. Spectral coherence at the semidiurnal frequency (Figure S1 in Supporting Information S1, bottom) is nearly unity. The sharp temperature decreases associated with the bore arrival are replicated well, although unfortunate gaps at the exact arrival time of the bores at 12:00 and 22:00 on 24 Jan are badly placed. Although clearly dominated by semidiurnal motions, both the CTD and fiber-inferred temperature time series are strongly non-sinusoidal, reminiscent of internal tide bores propagating upslope observed with similar methods at other steep topography sites (e.g., Alford et al., 2025; Klymak et al., 2011; Martini et al., 2013; van Haren and Gostiaux, 2012).

The fiber data show a complicated structure following each cold front, with one or more warm pulses occurring several hours after most of the fronts, with such pulse structures mostly absent in the CTD data. While data scarcity in the lower 5–10 m prevents a definitive assessment, we hypothesize that thin warm layers plunging downwards during upslope flow —resembling those seen in the model simulations of internal tides on super-critical slopes by Winters (2015)— could create such differences. Future experiments will instrument the bottom 10–15 m more densely in order to further explore the near-bottom dynamics, which are important for understanding abyssal circulation (Ferrari et al., 2016; Naveira Garabato, Spingys, Castro, et al., 2025).

The sharp cold fronts, which we interpret as the leading edge of internal bores propagating up the slope, are coherently traceable for several kilometers, particularly when plotted as temperature time rate of change (Figure 4). Speeds are calculated by visual fitting of the slope to selected features (dashed lines). The visually determined speeds are then compared (with nearly identical results) to speeds estimated from Radon transforms computed in 200-m by 1-hr windows following Butcher et al. (2021). For example, the cold front beginning near 15 km on 24 Jan at 0400 in Figure 3 initially propagates with a speed near 0.10 m s^{-1}, and speeds up and slows down twice before disappearing at about 10.5 km. The next bore, somewhat less than a tidal period later, is first seen at the seaward end of our extracted data, beginning at 0.05 m s^{-1}, speeding first to 0.12 m s^{-1} and eventually to 0.35 m s^{-1} (slanted dashed lines in Figures 3 and 4).

This speeding up of the bores as they climb the slope is seen for most bore features in both Figures 2 and 3, and follows expectations for a bore traveling at a speed $c_{bore} \sim NH$. Using the measured N profile and a bore height H of 100 m, consistent with the vertical extent of the sharpest cold fronts in the CTD observations in Figure 3 (top), one obtains expected speeds of 0.1, 0.15 and 0.35 m s^{-1} at 2,500, 1,700 and 1,000 m, respectively, approximately as observed.

Interestingly, the sharpest drops in temperature measured at the location of CTD station 3 are not associated with these "long-propagating" bores (which mostly do not reach that location), but rather with the set of arrivals approximately half a tidal period offset from them that appear around 10.5 km; for example, the feature beginning all the way at our observations' seaward end at about 10:00 on 24 January. Likely, these two sets of bores have different generation locations on the slope.

Figure 4 showcases the full complexity of the propagating and breaking waves (Figure 4). Viewing first the full time/along-cable record (top), the arrivals of the cold bores (sharp blue lines) at CTD station 3 alternate with

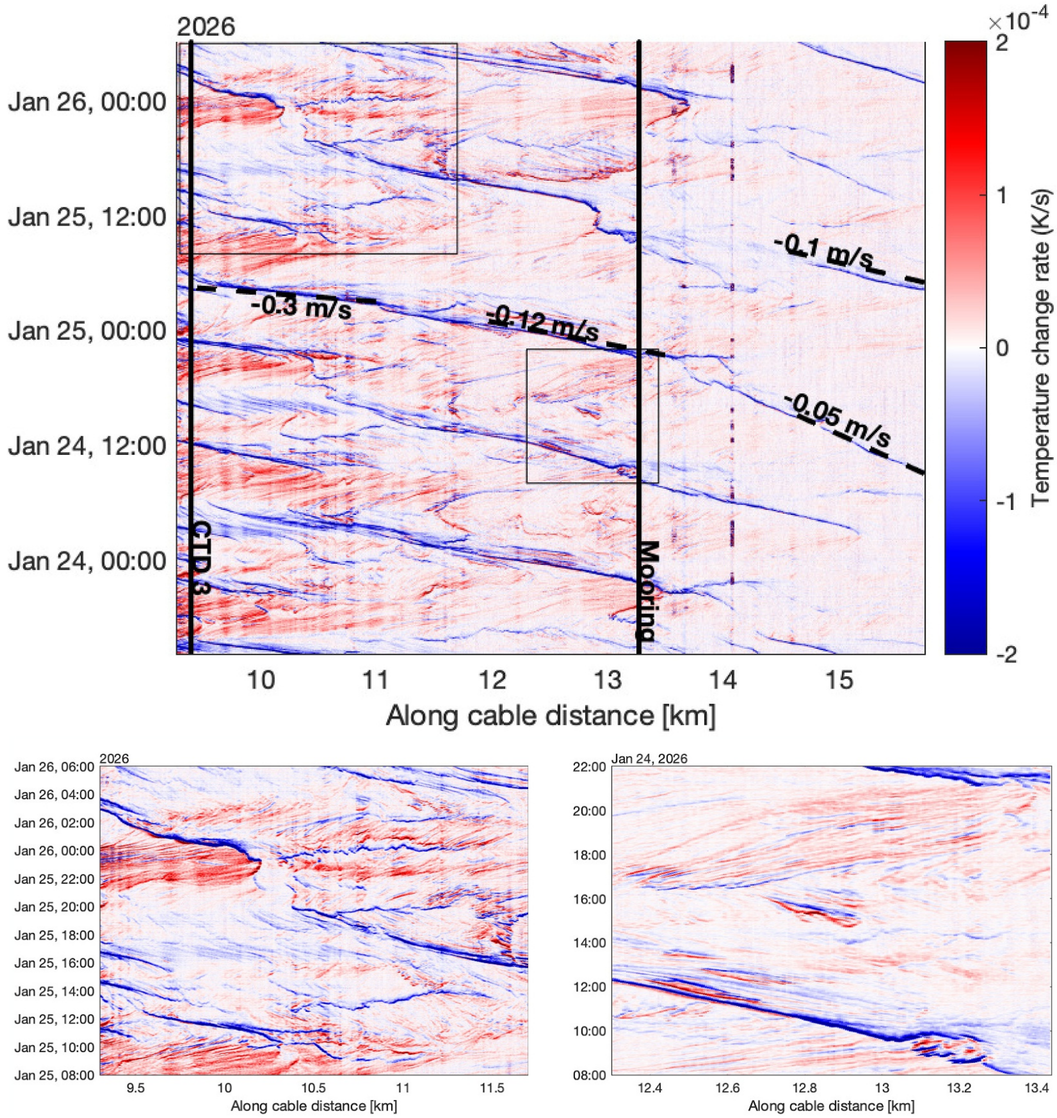

Figure 4. (Top) As in the bottom panel of Figure 3 but for the time derivative of fiber-inferred temperature $\partial T/\partial t$. Slanted dashed lines are representative propagation speeds. (bottom) Zoom-ins for the boxed regions indicated above.

seaward-propagating warming features, which again are reminiscent of the downslope motions seen in the Winters (2015) simulations. Zooming in on two representative periods (bottom panels), the observational challenge for a full understanding of the bore features is clear. Some of the onshore propagating signals have trailing secondary features (e.g., 12.55 km, 24 Jan at 12:00), while the offshore-propagating warming signals also at times have multiple crests and troughs. The latter may possibly be interpreted as advection of 3D wave features along the slope, as argued by Lucas and Pinkel (2022) using distributed temperature sensing (DTS) at a coastal site. That is, a wave structure with a leading edge aligned approximately along isobaths, but with crests and troughs behind it oriented perpendicular to isobaths, is advected sideways, giving apparent offshore propagation. Likely, the real situation is a combination of true offshore-propagating features as in Winters (2015), crossshore-advecting secondary waves as in Lucas and Pinkel (2022) and yet-to-be-determined types of wave and turbulent motions.

4. Summary and Discussion

These observations provide the first detailed validation of DAS-inferred near-bottom temperature variability against in situ CTD measurements reaching within 5–10 m of the seabed. Linear regressions yield an empirical temperature sensitivity $\partial\epsilon^*/\partial T$ of 21–37 μstrain K^{-1}, greater by a factor of 2.5–4 than the commonly used theoretical estimate described in Supporting Information S1. This discrepancy suggests that simple thermo-optic theory does not fully capture the response of installed seafloor telecommunication cables, likely due to a combination of thermal coupling, burial, and residual mechanically induced strain. This coefficient should be regarded as installation-specific and may vary with cable construction, burial, and coupling. Additionally, important questions remain regarding the spatial decorrelation scale for the empirical calibration coefficients.

With these caveats, the calibrated DAS record offshore of ≈km 8.25 reveals coherent semidiurnal internal tide bores propagating upslope and accelerating as stratification increases. Observed bottom temperature tendency measured from the fiber shows a wealth of complex wavelike and turbulence-like features. Together with the detailed temperature time series collected by the ship, observed features are indicative of the complex vertical structure of bottom boundary layers on slopes. Future work will seek to better resolve this near-boundary flow field just above the fiber.

Inshore of ≈km 8.25 (≈1,400 m depth) in Figure 2 (bottom), signals weaken and phase propagation disappears. Similar behavior is seen during the January data (not shown). Both behaviors are expected for internal tides on a supercritical slope, regardless of whether they are generated locally (Gayen & Sarkar, 2011) or remotely (Johnston et al., 2015; Zhao et al., 2018). Generation of baroclinic tidal motions is expected to occur at a so-called critical slope, where the bathymetric slope α matches the slope of an internal tide characteristic,

$$\gamma = \sqrt{\frac{\omega^2 - f^2}{N^2 - \omega^2}}. \quad (1)$$

Here, f is the inertial frequency, N is the buoyancy frequency, and ω is the frequency of the M_2 semidiurnal tide. Such a ray emanating from a near-critical region near 23 km (Figure 1c) would transit the subcritical deep portion of the slope between 16 and 23 km, and begin approaching the seafloor upon encountering the supercritical portion of the slope shoreward of that. Near the 1,300 m isobath, where the ray intersects the slope, it would be expected to reflect upward and seaward. Hence, the steepest part of the sloping topography appears to act as a wall that reflects internal tide energy back seaward. Although numerical modeling would be needed to confirm this simple explanation, similar behavior is seen at other supercritical slopes, such as Great Meteor Seamount (Gerkema & van Haren, 2007), Tasmania (Johnston et al., 2015; Zhao et al., 2018) and the heads of steep submarine canyons (Hamann et al., 2021). We therefore interpret the reduced amplitude and halted phase propagation in the fiber data shoreward of about 1,400 m as evidence of an internal tide propagating up a supercritical slope and reflecting seaward.

Together, our results demonstrate that combining distributed fiber sensing with targeted near-bottom profiling can provide unprecedented observational constraints on near-slope internal wave dynamics and boundary-layer variability. Future deployments incorporating denser near-bottom temperature and velocity measurements nearer to the fiber will help resolve the physical origin of the increased DAS temperature sensitivity, and enable quantitative estimates of internal tide energy conversion and turbulent mixing.

Conflict of Interest

The authors declare no conflicts of interest relevant to this study.

Availability Statement

All data presented in this paper are available at Alford et al. (2026).

Acknowledgments

We thank the engineers of the Multiscale Ocean Dynamics group, the scientists and engineers at the Madeira ARDITI institute and the captain, crew and technical support team of *RRS Discovery*. Without the hard work and skill of all of these people, the observations would not have been possible. We are also grateful to the volunteers who participated in the cruises: Shriya Fruitiwala, Alex Roberts, Arianna Ferrotti, Kate Oglethrope, Naina Shah, Daniel Heathcote, Fran Gomes, Tianshu Liu, Amir Atoufi and Amanda Geller. This work was supported by the US National Science Foundation under awards OCE-2320944 (SIO) and OCE-2320945 (NPS), and the UK National Environmental Research Council (NERC) under awards NE/Y003365/1, NE/Z000408/1 and NE/Y005589/1. We also thank Emacom and EllaLink for their vision in adding a dark fiber to the seafloor cable used here, and Emacom for granting access to their facilities and providing support for the operation of GeoLab. We acknowledge FCCN, FCT, and Géant for providing connectivity, and INESC-TEC for data storage. A.L. acknowledges support from the ECHO project (https://doi.org/10.54499/2024.13655.PEX), the SUBMERSE EU project (GA 101095055), and FCT, I.P./MCTES through national funds (PIDDAC): LA/P/0068/2020 (https://doi.org/10.54499/LA/P/0068/2020), UID/50019/2025 (https://doi.org/10.54499/UID/50019/2025), UID/PRR/50019/2025 (https://doi.org/10.54499/UID/PRR/50019/2025), UID/PRR2/50019/2025 (https://doi.org/10.54499/UID/PRR2/50019/2025), and Advanced Research and Invention Agency (SCOP-PR01-P019).

References

Alford, M. H., Belal, M., Naveira Garabato, A. C., Spingys, C., Voet, G., Godin, O. A., et al. (2026). Madeira groundtruthing project data repository [Dataset]. *Scripps Institution of Oceanography, University of California San Diego*. Retrieved from https://mod.ucsd.edu/data

Alford, M. H., Wynne-Cattanach, B., Boyer, A. L., Couto, N., Voet, G., Spingys, C. P., et al. (2025). Buoyancy flux and mixing efficiency from direct, near-bottom turbulence measurements in a submarine canyon. *Journal of Physical Oceanography*, *55*, 97–118.

Budiansky, B., Drucker, D. C., Kino, G. S., & Rice, J. R. (1979). Pressure sensitivity of a clad optical fiber. *Applied Optics*, *18*(24), 4085–4088. https://doi.org/10.1364/AO.18.004085

Butcher, A., Hudson, T. S., Kendall, J. M., Kufner, S.-K., Brisbourne, A. M., & Stork, A. L. (2021). Radon transform-based detection of microseismicity on DAS networks: A case study from Antarctica. In *EAGE GeoTech 2021 second EAGE workshop on distributed fibre optic sensing* (Vol. 2021, pp. 1–4). European Association of Geoscientists & Engineers. https://doi.org/10.3997/2214-4609.202131039

Ferrari, R., Mashayek, A., McDougall, T. J., Nikurashin, M., & Campin, J. M. (2016). Turning ocean mixing upside down. *Journal of Physical Oceanography*, *7*, 2239–2261. https://doi.org/10.1175/jpo-d-15-0244.1

Gayen, B., & Sarkar, S. (2011). Boundary mixing by density overturns in an internal tidal beam. *Geophysical Research Letters*, *38*(14), L14608. https://doi.org/10.1029/2011gl048135

Gerkema, T., & van Haren, H. (2007). Internal tides and energy fluxes over great meteor seamount. *Ocean Science Discussions*, *4*, 371–398.

Godin, O. A. (2006). Recovering the acoustic Green's function from ambient noise cross correlation in an inhomogeneous moving medium. *Physical Review Letters*, *97*(5), 054301. https://doi.org/10.1103/physrevlett.97.054301

Gräff, D., Lipovsky, B. P., Vieli, A., Dachauer, A., Jackson, R., Farinotti, D., et al. (2025). Calving-driven fjord dynamics resolved by seafloor fibre sensing. *Nature*, *644*(8076), 404–412. https://doi.org/10.1038/s41586-025-09347-7

Hamann, M. M., Alford, M. H., Lucas, A. J., Waterhouse, A. F., & Voet, G. (2021). Turbulence driven by reflected internal tides in a supercritical submarine canyon. *Journal of Physical Oceanography*, *51*(2), 591–609. https://doi.org/10.1175/jpo-d-20-0123.1

Hartog, A., Conduit, A., & Payne, D. (1979). Variation of pulse delay with stress and temperature in jacketed and unjacketed optical fibres. *Optical and Quantum Electronics*, *11*(3), 265–273. https://doi.org/10.1007/BF00620112

Hocker, G. B. (1979). Fiber-optic sensing of pressure and temperature. *Applied Optics*, *18*(9), 1445–1448. https://doi.org/10.1364/AO.18.001445

Johnston, T. M. S., Rudnick, D. L., & Kelly, S. M. (2015). Standing internal tides in the Tasman Sea observed by gliders. *Journal of Physical Oceanography*, *45*(11), 2715–2737. https://doi.org/10.1175/jpo-d-15-0038.1

Klymak, J. M., Alford, M. H., Pinkel, R., Lien, R. C., Yang, Y. J., & Tang, T. Y. (2011). The breaking and scattering of the internal tide on a continental slope. *Journal of Physical Oceanography*, *41*(5), 926–945. https://doi.org/10.1175/2010JPO4500.1

Loureiro, A., Schlaphorst, D., Matias, L., Pereira, A., Corela, C., Gonçalves, S., & Caldeira, R. (2025). First DAS observations from the GeoLab fibre in Madeira, Portugal. *Seismica*, *4*(2). https://doi.org/10.26443/seismica.v4i2.1482

Lucas, A. J., & Pinkel, R. (2022). Observations of coherent transverse wakes in shoaling nonlinear internal waves. *Journal of Physical Oceanography*, *52*(6), 1277–1293. https://doi.org/10.1175/jpo-d-21-0059.1

Martini, K. I., Alford, M. H., Kunze, E., Kelly, S. M., & Nash, J. D. (2013). Internal bores and breaking internal tides on the Oregon continental slope. *Journal of Physical Oceanography*, *43*(1), 120–141. https://doi.org/10.1175/jpo-d-12-030.1

Naveira Garabato, A. C., Spingys, C. P., Castro, B. F., Couto, N., Drake, H. F., Forryan, A., et al. (2025). Connecting mixing to upwelling along the ocean's sloping boundary. *Geophysical Research Letters*, *52*(22), e2025GL119186. https://doi.org/10.1029/2025gl119186

Naveira Garabato, A. C., Spingys, C. P., Lucas, A. J., Dotto, T. S., Wild, C. T., Tyler, S. W., et al. (2025). Distributed optical fibre sensing in physical oceanography: Emergence and future prospects. *EGUsphere*, *2025*, 1–49.

Pelaez Quiñones, J. D., Sladen, A., Ponte, A., Lior, I., Ampuero, J.-P., Rivet, D., et al. (2023). High resolution seafloor thermometry for internal wave and upwelling monitoring using distributed acoustic sensing. *Scientific Reports*, *13*(1), 17459. https://doi.org/10.1038/s41598-023-44635-0

Sidenko, E., Tertyshnikov, K., Lebedev, M., & Pevzner, R. (2022). Experimental study of temperature change effect on distributed acoustic sensing continuous measurements. *Geophysics*, *87*(3), D111–D122. https://doi.org/10.1190/geo2021-0524.1

Sinnett, G., Davis, K. A., Lucas, A. J., Giddings, S. N., Reid, E., Harvey, M. E., & Stokes, I. (2020). Distributed temperature sensing for oceanographic applications. *Journal of Atmospheric and Oceanic Technology*, *37*(11), 1987–1997. https://doi.org/10.1175/JTECH-D-20-0066.1

Spingys, C. P., Naveira Garabato, A. C., & Belal, M. (2024). Distributed optical fibre sensing for high space-time resolution ocean velocity observations: A case study from a macrotidal channel. *Earth and Space Science*, *11*(5), e2023EA003315. https://doi.org/10.1029/2023ea003315

van Haren, H., & Gostiaux, L. (2012). Energy release through internal wave breaking. *Oceanography*, *25*(2), 124–131. https://doi.org/10.5670/oceanog.2012.47

Williams, E. F., Ugalde, A., Martins, H. F., Becerril, C. E., Callies, J., Claret, M., et al. (2023). Fiber-optic observations of internal waves and tides. *Journal of Geophysical Research: Oceans*, *128*(9), e2023JC019980. https://doi.org/10.1029/2023jc019980

Winters, K. B. (2015). Tidally driven mixing and dissipation in the stratified boundary layer above steep submarine topography. *Geophysical Research Letters*, *42*(17), 7123–7130. https://doi.org/10.1002/2015GL064676

Wu, W., Zhan, Z., Peng, S., Ni, S., & Callies, J. (2020). Seismic ocean thermometry. *Science*, *369*(6510), 1510–1515. https://doi.org/10.1126/science.abb9519

Zhao, Z., Alford, M. H., Simmons, H. L., Braznikov, D., & Pinkel, R. (2018). Satellite investigation of the M2 internal tide in the Tasman Sea. *Journal of Physical Oceanography*, *48*(3), 687–703. https://doi.org/10.1175/jpo-d-17-0047.1